Temperature- and current-dependent dephasing in an Aharonov-Bohm ring

Kuan-Ting Lin, Yiping Lin, C. C. Chi, and J. C. Chen
Department of Physics, National Tsing Hua University, Hsinchu 30013, Taiwan

T. Ueda and S. Komiyama
Department of Basic Science, University of Tokyo, Komaba, Tokyo 153-8902, Japan

(Received 19 August 2009; revised manuscript received 8 November 2009; published 8 January 2010)

We investigate the dependence of the dephasing rate in a ballistic Aharonov-Bohm ring on the temperature T, the bias current, and the probe configuration. We find that the probe configuration influences the conductance but not the dephasing rate. Rather, averaging of the transmission phase, carried by thermally excited or current-induced electrons results in dephasing. We find that the appropriate energy window responsible for the dephasing is set by the drift velocity of the interfering electrons and the asymmetry of the ring path.

DOI: 10.1103/PhysRevB.81.035312 PACS number(s): 73.23.Ad, 73.63.Nm

I. INTRODUCTION

When an electron circulates in an external magnetic field, it can accumulate an additional electronic phase between interfering paths due to the Aharonov-Bohm (AB) effect. This causes magnetoresistance oscillations with a flux periodicity of $\Phi_0=h/e$. Experimentally, AB oscillations were demonstrated by Webb *et al.*[1] in disordered metal rings and by Timp *et al.*[2] in semiconductor rings. Following these pioneering experiments, two decades of research on mesoscopic ring structures displaying the AB effect have revealed rich information on the phase states of carriers. Such experiments have also gradually emerged as useful tools to study various phase-related physical problems.[3–9]

Dephasing processes are among the most essential of issues when studying these mesoscopic systems. Decoherence suppresses quantum interference effects, and leads to a reduction in the visible amplitude of the AB oscillation. The loss of phase coherence at low temperatures in disordered conductors has been investigated extensively.[10] The main mechanisms responsible for decoherence in the low-temperature regime include electron-electron scattering[11] and thermal averaging.[12] The first mechanism is a phase-breaking process involving transfer of small amounts of momentum and energy via scattering events, and it is caused by the interaction of an electron carrier with other nearby electrons through the fluctuating electric field.[13] The second mechanism deals with temperature-induced phase shifts. For an interferometer with two asymmetric paths, a geometrical phase difference $\Delta(k_F L)$ exists, where k_F is the Fermi wave vector and L is the length of one arm of a ring. This phase difference changes as a function of the Fermi energy E_F. Thermal averaging effects dominate when the temperature scale falls within the relevant energy window.

Dephasing processes in ballistic mesoscopic conductors are more poorly understood. The two mechanisms important in diffusive systems as described above are still valid; nevertheless, one should expect key differences in the behavior of AB oscillations. In ballistic conductors, interchannel and boundary scattering become important; moreover, because of the poor-screening effect inside the conductor, the transport characteristics should strongly depend on the specific process whereby a carrier enters or leaves the system.[14,15] A number of experiments have measured the dephasing rate in ballistic quantum dots[16–20] and rings.[21–24] The dephasing rate is extracted from the temperature (T) dependence of the AB oscillation amplitude. For ballistic rings, it is found that the AB amplitude ΔR_{AB} decrease with T according to the relationship $\Delta R_{\mathrm{AB}} \propto \exp(-\tau_L/\tau_\phi(T))$. Here the dephasing rate τ_ϕ^{-1} is proportional to T. τ_L is the transit time of electrons through a ring arm and is equivalent to L/v_F, where v_F is the Fermi velocity. τ_ϕ is the quantum phase coherence time.[23,24]

Recently Seelig *et al.*[15,25] proposed a phase-breaking mechanism. They investigated the dephasing rate in an AB ring coupled to a pair of side gates. Experimentally, side gates are commonly placed in the vicinity of an AB ring, to tune the electron phases. Their theory concluded that the principal source of dephasing is the fluctuation of internal potentials induced by charge fluctuations between the gates and the arms of the ring. The resulting dephasing rate is linearly dependent on temperature and depends on the probe configuration. Seelig *et al.*'s theory agrees with recent experiments.[23–25]

In this paper, we report on our study of the dephasing rate in a ballistic AB interferometer. To clarify the sources of dephasing, no gate is near the arm of the ring. Hence, our device should suffer less from the charge-fluctuation-induced dephasing theorized by Seelig *et al.* We measure the dependence of ΔR_{AB} on the temperature and on the bias current I in different probe configurations. Our results reveal that τ_ϕ^{-1} is proportional to T as is consistent with previous studies; however, we find that the dephasing rate is insensitive to the measurement configuration. Increasing I strongly reduces the AB oscillation amplitude. Our results suggest that the energy averaging effect of thermal excitation and the energy spreading due to bias is responsible for the phase decoherence.

II. EXPERIMENTAL RESULTS AND ANALYSIS

A. Experiments

Figures 1(a) and 1(b) illustrate the device under study. The device consists of an AB ring defined on a GaAs/AlGaAs heterostructure containing a two-dimensional electron gas (2DEG). The wafer, grown by conventional

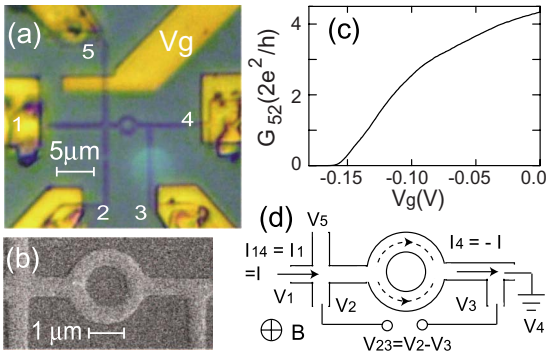

FIG. 1. (Color online) (a) An optical micrograph of one of the devices used in the experiment. (b) SEM micrograph of the ring structure. (c) The two-probe conductance G_{52} vs V_g. Since V_g is less than ~ -0.16 V, contact 5 is isolated from the device. (d) A diagram illustrating our notation of currents and voltages in an example of a five-terminal local measurement. Here $R_{14,23}=V_{23}/I_{14}$. The current drain is connected to the circuit ground.

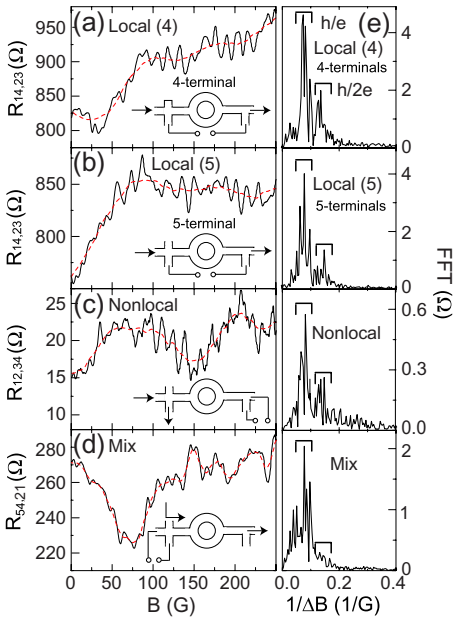

FIG. 2. (Color online) Magnetoresistance of the ring as measured in different probe configurations. (a) Four-terminal local setup ($V_g=-0.18$ V, current: $1\rightarrow4$, voltage: $2\rightarrow3$) (b) Five-terminal local setup ($V_g=0$ V, current: $1\rightarrow4$, voltage: $2\rightarrow3$) (c) Five-terminal nonlocal setup ($V_g=0$ V, current: $1\rightarrow2$, voltage: $3\rightarrow4$) (d) Five-terminal mixed setup ($V_g=0$ V, current: $5\rightarrow4$, voltage: $1\rightarrow2$). The dashed red line through the oscillations on each trace is the background resistance, R_{back}. (e) The Fourier spectrum of the data in Figs. 2(a)–2(d), after subtracting R_{back}. The bars indicate the ranges of inverse field which include h/e and $h/2e$ peaks.

molecular-beam epitaxy, has a 2DEG situated 80 nm below the surface. The ring pattern is fabricated using standard e-beam lithography (EBL) and is transferred to the 2DEG using a 40 nm shallow wet etch. The inner diameter of the ring is ~ 1.37 μm and the effective widths of the arms ~ 470 nm. The convention for labeling the leads is shown in Fig. 1(a). Using a second EBL step with assistance from metal alignment marks, a Au/NiCr gate is defined cross the path to the contact 5. The two-terminal conductance G_{52} is illustrated in Fig. 1(c) and demonstrates the functionality of the cross gate. By applying a negative voltage V_g to the gate, the device geometry can be altered from a five to a four terminal device.

Measurements are made in a dilution fridge with a base temperature of ~ 25 mK. The magnetoresistance is measured using conventional lock-in techniques with a low-frequency ac excitation current at 17 Hz. The current excitation is typically less than 10 nA, unless the effects of current are being explicitly probed. The four-probe magnetoresistance measured in different probe configurations is denoted by $R_{mn,kl} \equiv (V_k - V_l)/I_{mn} = V_{kl}/I_{mn}$, for current contacts m, n and voltage probes k, l [see Fig. 1(d)]. The carrier density deduced from Shubnikov-de Haas oscillations is $n=2.8\times10^{11}$ cm^{-2} and the mobility is $\mu=3.0\times10^5$ cm^2/Vs at 4.2 K. The corresponding conductance of the ring is approximately 17 times the fundamental unit of conductance, suggesting the presence of ~ 17 channels in the wire. The mean free path is approximately 3 μm. Note that one salient feature of our device is that the contact leads are made closed to the ring structure, such that the device size (~ 15 μm) is less than the phase coherence length. A total of three samples are measured in this work, and all samples reproduce the main features regardless the thermal cycles. However, for economy, the experimental results presented in this paper are obtained from one sample.

B. Dephasing in different probe configurations

In this section, we present our study of the dephasing rate as a function of different probe configurations. For different configurations, we change only how the voltmeter and the current source are connected to the device in the external circuit, as displayed in the insets in Figs. 2(a)–2(d). These configurations are four-terminal local, five-terminal local, nonlocal, and mixed setup, respectively. Local vs nonlocal configuration is defined in the view of classical circuitry, as current passing vs not passing through the ring, and voltage probes crossing vs not crossing the ring

The resistance $R_{mn,kl}$ measured in various probe configurations in a perpendicular magnetic field B is shown in Figs. 2(a)–2(d). Visible AB oscillations $R_{\rm AB}$ are superposed on a slowly varying resistance background R_{back}, so that $R_{mn,kl}=R_{\rm AB}+R_{back}$. The fast Fourier transforms (FFT) of magnetoresistances after subtracting R_{back} are shown in Fig. 2(e). In all configurations, Fourier spectra reveal periods of both h/e and $h/2e$. Those peaks associated with the $h/2e$ period appear as smaller bumps. The oscillation period of the h/e peak is about 14 G corresponding to a 1.9 μm annuli which matches the average size of the ring, as estimated from Fig. 1(b).

The magnitude of the AB oscillation amplitude, $\Delta R_{\rm AB}$, which quantifies the degree of coherence, is obtained by integrating the h/e FFT peaks within the bar as indicated in Fig. 2(e). $R_{mn,kl}$ varies depending on the measurement configuration. In the five-terminal geometry the ratios of $\Delta R_{\rm AB}$ to $R_{mn,kl}$ are approximately 1.1–1.3 %, 8–13.3 %, and 1.8–2.3 % for local, nonlocal, and mixed setup, respectively. Among the three-probe-configurations studied, $\Delta R_{\rm AB}$ of the

nonlocal setup is smallest, but appears most visible due to suppression of the background signal.

To qualitatively evaluate the probe dependence of $R_{mn,kl}$ and ΔR_{AB}, we apply the Landauer-Büttiker (LB) formalism.[26,27] For a phase-coherent conductor with arbitrary number of leads N, the selection of pairs of voltage and current probes can give different conductance. The LB formalism gives a general rule to obtain the voltages V_m and currents I_m which appear in the lead m

$$I_m = \frac{2e^2}{h} \sum_{n,n\neq m}^{N} (T_{nm}V_m - T_{mn}V_n). \tag{1}$$

T_{mn} represents the transmission probability of an electron passing from lead m into lead n. In a generalized LB formula, the T_{mn} can be treated as the thermally averaged transmission coefficients including both coherent and incoherent components. From the device geometry shown in Fig. 1(a), we assume $T_{12}=T_{21}=T_{51}=T_{15}=T_{43}=T_{34}=T_0$, $T_{13}=T_{31}=T_{42}=T_{24}=T_{54}=T_{45}=T_1$, $T_{23}=T_{32}=T_{41}=T_{14}=T_{53}=T_{35}=T_2$, and $T_{52}=T_{25}=T_3$. Based on symmetry considerations, we further approximate $T_3 > T_0 \gg T_1 \geq T_2$. With the above approximations, in a five-terminal device ($N=5$) the LB formalism predicts resistances of

$$R_{14,23} = \left(\frac{h}{e^2}\right)\frac{T_0^2(T_0+2T_3)}{D}, \tag{2}$$

$$R_{12,34} = \left(\frac{h}{e^2}\right)\frac{(T_1^2-T_2^2)(T_0+2T_3)}{D}, \tag{3}$$

$$R_{54,21} = \left(\frac{h}{e^2}\right)\frac{2T_0T_1(T_3-T_0)}{D} \tag{4}$$

for the local, the nonlocal, and the mixed setups, respectively. Here the denominator D is the subdeterminant of the matrix defined by Eq. (1), which can be simplified as

$$D = 3T_0^2(T_0+2T_3)(T_1+T_2) + T_0T_3(6T_1^2+14T_1T_2+6T_2^2) + T_0^2(6T_1^2+13T_1T_2+6T_2^2).$$

Equation (3) indicates that the lower nonlocal resistance, $R_{12,34}$, results from difference term T_1-T_2. Moreover, by examining Eqs. (2)–(4) we can readily see that $R_{14,23} > R_{54,21} > R_{12,34}$, in good qualitative agreement with the observations shown in Figs. 2(b)–2(d).

For both the four- and five-terminal configuration, ΔR_{AB} is approximately 10.5 Ω using the local setup [see Fig. 2(e)] and approximately 2.2 Ω in the nonlocal setup. To evaluate the effects of contacts and device geometry on decoherence, Fig. 3(a) illustrates the evolution of AB oscillations with changing V_g. By biasing V_g, the coupling strength of contact 5 to the ring can be continuously tuned. The subtracted background resistance R_{back} is shown in Fig. 3(b). The dependence of the oscillation amplitude ΔR_{AB} on V_g is summarized in Fig. 3(c). The results reveal that, within experimental error, ΔR_{AB} is insensitive to variations in background resistance, and the contact 5 does not induce significant phase breaking. It is interesting to note that sudden π-phase jumps are observed when applying V_g. However, the proposed

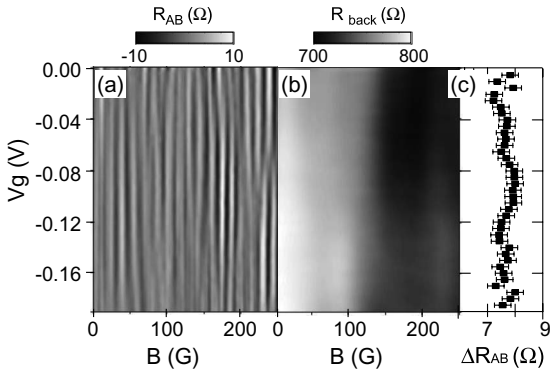

FIG. 3. The evolution of AB amplitudes going from a five-terminal to a four-terminal ring by applying $V_g=0$ to −0.19 V in the local configuration. The data were taken in different cooling from Fig. 2. (a) Gray-scale plot of the AB oscillation component R_{AB} as a function of V_g and B. (b) Gray-scale plot of the subtracted background resistance R_{back}. (c) The gate dependence of AB oscillation amplitudes ΔR_{AB}, obtained by FFT analysis of R_{AB}.

mode switching mechanism is unexpected in the present experiment.[28] The origin of this phase shift is unclear.

To investigate the dephasing rate in different probe configurations, the temperature dependence of the AB amplitude is illustrated in Fig. 4. The AB oscillation amplitudes of the h/e peaks saturate as the temperature drops below about 100 mK, irrespective of the device geometry and the probe configuration. The origin of the saturation of the dephasing rate near the zero-temperature limit has been widely debated in recent years[10] and is not resolved here. We focus on the dephasing rate above 150 mK. An empirical relation for the temperature dependence of ΔR_{AB} is

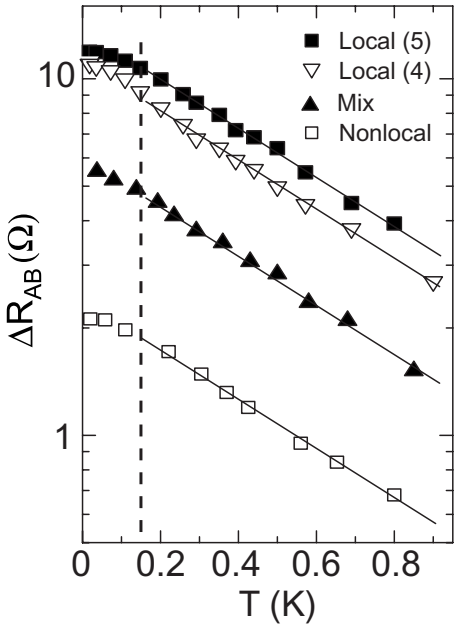

FIG. 4. Temperature dependence of the AB amplitude ΔR_{AB} for various probe configurations. The solid lines are the results of fitting the data using exponential relationship as in Eq. (5). The dashed line marks the onset of linear fit. ΔR_{AB} saturates for the temperatures below the dashed line.

TABLE I. The exponent b (K^{-1}) extracted from the fitted data in Fig. 4.

Configuration	Local (4)	Local (5)	Nonlocal	Mix
b	1.59 ± 0.04	1.63 ± 0.06	1.56 ± 0.05	1.63 ± 0.04

$$\Delta R_{AB} = a \exp(-bT), \tag{5}$$

where a and b are fitting parameters. The solid lines shown in Fig. 4 are fitted using Eq. (5). The dephasing rate can be extracted from parameter b, using the relation $\tau_\phi^{-1} \propto b$. The fitting results of b are summarized in Table I. For all measurement configurations the values of b are around 1.6. Within the experimental error (approximately 1 Ω in ΔR_{AB}), our data indicate that dephasing is independent of probe configuration.

The phase coherence length L_ϕ can be estimated from $\exp(-L/L_\phi) = \exp(-bT)$.[23] With the average $L \sim 2.9$ μm and $b \sim 1.63$ in the five-terminal local-probe configuration, we deduce $L_\phi \sim 17.8$ μm at $T = 100$ mK. Thus, L_ϕ exceeds the device size (~ 15 μm). Our device could be viewed as a ballistic conductor with good phase coherence at low temperatures.

In the case of ballistic transport in a coherent mesoscopic conductor, the arrangement of the voltage and current leads only results in different conductance, but electron coherence of remains the same.[27] Dephasing due to probe configuration changes can only occur when a path-dependent phase-destroying event occurs in the interference path. In previous works, the specific dephasing source is the voltage fluctuations caused by accumulated charges between the gates and the ring path.[24,25] Our data as shown in Fig. 4 confirm that without external gates near the ring, the decoherence is insensitive to the probe methods.

The effects of thermal averaging effect can be estimated by $bT = \tau_L k_B T/\hbar$, with b approximately 1.5 K^{-1}, where k_B is Boltzmann's constant. This is comparable with our findings. Thermal averaging effects are sufficient to account for the observed dephasing in the present case.

C. Current-dependent dephasing

Next we investigate the effect of current on decoherence. Temperature dependent on AB oscillation amplitudes extracted from local and nonlocal measurements for different biasing currents are shown in Figs. 5(a) and 5(b), respectively. With increasing I, ΔR_{AB} remains saturated for temperatures below $T < 100$ mK, but the saturated values rapidly drops. As the lattice temperatures rise, ΔR_{AB} exponentially decreases; however, the damping factor b becomes smaller at higher I, as shown in the insets of Fig. 5. Simple electron heating due to applied current cannot explain these results. In the case of heating, one would expect the exponent b to increase and the phase saturation to disappear, due to the elevation of electronic temperatures by excess currents. The dependence of b on I suggests that to deduce b as the decoherence rate is no longer adequate in the present case. Current-induced dephasing effects must be taken into account in Eq. (5).

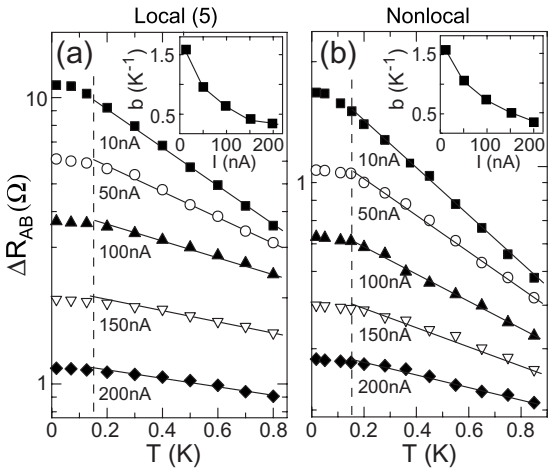

FIG. 5. Temperature dependence of the AB amplitude ΔR_{AB} for different currents in a five-terminal configuration. (a) Local setup. (b) Nonlocal setup. The solid lines are fits using Eq. (5) in the temperature interval covered by the line. ΔR_{AB} approaches a saturation value for temperatures below the dashed lines. Values of the fit parameter b are shown in the insets with error bars comparable to the symbol size.

Importantly, the current dependence of b is also insensitive to probe configuration [see insets in Figs. 5(a) and 5(b)]. This suggests that current-induced dephasing could be a genuine process, with an origin related to the thermal averaging effect. To explain the data shown in Fig. 5, we extend the thermal averaging effect to the nonlinear transport regime. We start by considering the transport properties of a two-terminal multichannel AB interferometer.[26] The various transmission probabilities can be expressed as $T_{ij} = \alpha_{ij} + \beta_{ij} \cos(2\pi\Phi/\Phi_0 + \theta_{ij})$, where each T_{ij} is specifically the probability of a wave entering through channel j and leaving through channel i. Here β_{ij} represents the AB oscillation amplitude, α_{ij} represents the nonoscillatory component, θ_{ij} accounts for phase variation, $\Phi_0 = h/e$ is the flux quantum, and Φ is the magnetic flux through the annulus. If the T_{ij} are small, we can simply sum over all incident and transmitted channels and obtain the overall transmission probability $T(E) = \Sigma T_{ij}$.[26] Next, we assume that $\theta_{ij} = \Delta(kL)$, to account for the phase accumulated through asymmetric ring paths. Neglecting the effect of electron interaction, we rearrange the summation items and expend the wave vector $k(E)$ to first order in the energy E around the Fermi energy E_F. Then $T(E)$ becomes

$$T(E) = T_0 + T_1 \cos\left[k_F \Delta L + \frac{E - E_F}{E_c} + 2\pi\frac{\Phi}{\Phi_0}\right], \tag{6}$$

where $E_c = 2E_F/(k_F \Delta L)$, ΔL is the difference in length between the two arms, k_F is the Fermi wave vector, T_0 represents the nonoscillatory terms, and T_1 represents the AB oscillation terms.[29] The nonlinear conductance at finite temperature can be expressed as $I = (2e/h)\int T(E)[f_S(E) - f_D(E)]dE$. Here, $f_{S,D}(E) = 1/(1 + \exp[(E - \mu_{S,D})/k_B T])$ is the Fermi-Dirac distribution, where $\mu_S = E_F + eV$ and $\mu_D = E_F$ are the chemical potentials evaluated for the source and drain contacts, respectively. We thus obtain

$$I = \frac{2e}{h}\left\{ T_0 eV + T_1(2\pi k_B T)\mathrm{csch}\left(\frac{k_B T\pi}{E_c}\right)\sin\left(\frac{eV}{2E_c}\right) \times\cos\left[\frac{eV}{2E_c} + \frac{2E_F}{E_c} + 2\pi\frac{\Phi}{\Phi_0}\right]\right\} \quad (7)$$

From Eqs. (6) and (7), it is clear that E_c represents a characteristic energy. As $V\to 0$ and $k_BT \gg E_c$ in Eq. (7), the AB amplitude decays exponentially, which is consistent with Eq. (5). The strength of the AB amplitudes can be conveniently quantified using the visibility, defined as $\nu=(I_{max}-I_{min})/(I_{max}+I_{min})$

$$\nu = \nu_0\left(\frac{k_BT}{eV}\right)\mathrm{csch}\left(\frac{k_BT}{E_c}\right)\sin\left(\frac{eV}{2E_c}\right), \quad (8)$$

where $\nu_0=2\pi T_1/T_0$. The visibility is dependent on the interplay of the energy scales k_BT, eV, and E_c. A phase difference of E/E_c is accumulated as an electron with energy E travels through an asymmetric ring. This phase is k_BT/E_c if thermally induced and is eV/E_c if induced by bias voltage. Averaging over these phases for interfering electrons whose energy are spreading over the windows E_c, leads to a reduction in AB oscillation amplitude. It is intriguing to note that the visibility derived in Eq. (8) depends on voltage, temperature, and asymmetry in a manner comparable to an electrical Mach-Zehnder interferometer, employed by the edge channels in the integer quantum Hall regime.[30] Noting this coincidence, we infer the universality of the functional form of the visibility, and extend Eq. (8) to a multiterminal mesoscopic conductor. To do so, we must redefine $V=V_{mn}$, i.e., ν is only relevant to the voltage difference between voltage probes m and n. Making this change, we can evaluate ν for different probe configurations.

To compare Eq. (8) with our experimental results, we define $\nu=\Delta R_{AB}/R_{mn,kl}(B\to 0)$. V_{mn} can be determined by V-I curves at $B=0$ T as shown in Fig. 6(c). ν_0 and E_c are used as fitting parameters. The solid lines illustrated in Figs. 6(a) and 6(b) are the fitting results for local and nonlocal measurements, respectively. The visibility of the nonlocal measurement is larger than that of the local measurement due to $R_{14,23}>R_{12,34}$, as discussed earlier. The functional dependence of ν on T and V corresponds well with the experimental results for $T>150$ mK. Equation (8) predicts that ν tends to approach ν_0 in the low-temperature limit as $eV \ll E_c$. It is interesting to compare the experimentally measured visibility to the calculated one as $k_BT \leq E_c$. We found that the temperature dependence of the calculated ν can quantitatively trace the experimental data, but the slight deviation occurs at low bias current as $I \leq 50$ nA. The discrepancy in this case could be understood if the electron temperature actually is higher than the lattice temperature as $T \leq 100$ mK. Therefore, the flatness of ν measured at low temperatures is likely due to the saturation of the electron temperatures.

The fitting parameters ν_0 and E_c for both local and nonlocal probe configurations are summarized in Figs. 6(d) and 6(e). There exist a number of striking consistencies in ν_0 and E_c between the local and nonlocal setups. First, E_c increases monotonically with applied current, and its value is remarkably consistent over different probe methods. This provides

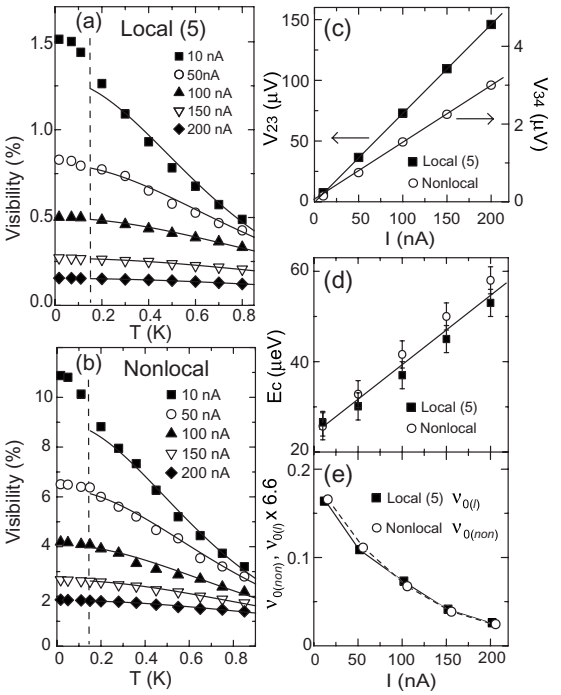

FIG. 6. The visibility of AB oscillations for various biasing currents in (a) the local setup, and (b) the nonlocal setup. The solid lines are least-squares fits of Eq. (8) to the data for $T>100$ mK. (c) Voltage vs current characteristics for local (V_{23} left axis) and nonlocal (V_{34} right axis) measurements. The fitted parameters (d) E_c and (e) ν_0, where $\nu_{0(l)}$ and $\nu_{0(non)}$ represent the visibility for the local and nonlocal setups, respectively.

strong evidence that E_c represents a genuine energy scale related to the decoherence rate. E_c can be rewritten as $E_c=\hbar v_d/\Delta L$, where v_d is the drift velocity. Therefore, the current dependence of E_c can be explained as the increase of the drift velocity with increasing electric field. Based on the inner and outer perimeters of the ring annulus, we estimate ΔL is about 1.6–0.2 μm [see Fig. 1(b)]. From this, we can deduce that v_d is approximately $1.1-0.1\times 10^7$ cm/s, consistent with previous reports.[31] Furthermore, k_B/E_c, approximately 1.4–3.4 K^{-1} is also comparable to the experimentally determined b. Lastly, the visibility measured in local $\nu_{0(l)}$ versus nonlocal $\nu_{0(non)}$ configurations can be related by $\nu_{0(non)}\sim 6.6\times\nu_{0(l)}$, as shown in Fig. 6(e). This scaling can be understood as the ratio of the oscillatory transmission in $R_{14,23}/R_{12,34}$, as obtained by Eq. (1). For a detailed quantitative discussion of ν_0, a more complete multichannel and multiprobe Landauer formula must be considered.[32]

The consistency of E_c and the scaling of ν_0 using different probe configurations strongly validates the stated functional dependence of ν on T and V. Our result provides a unified picture of dephasing for a multiterminal and multichannel ballistic conductor, wherein decoherence is governed by the averaging of the phases of the excited electrons circulating across asymmetric ring paths.

III. CONCLUSIONS

In summary, we have measured the temperature and current dependences of phase breaking in a ballistic five-

terminal AB ring. In this work, there is no metal gate in the vicinity of the ring path, so environmental effects on the dephasing are minimized. This enables us to probe the basic properties of phase breaking. We conclude that the decoherence rate is insensitive to probe configuration. Moreover, we find an energy scale E_c responsible for the temperature and current dependences of AB oscillations. E_c is the result of intrinsic asymmetry of two ring arms, and it characterizes an energy window of dephasing. We thus derive a general functional form for the visibility, accounting for the role of phase differences due to temperature, bias voltage and asymmetric geometry. We successfully apply this to interpret our experimental data.

ACKNOWLEDGMENTS

We acknowledge A. M. Chang, Chung-Yu Mou, and Po-Chung Chen for helpful discussions. J.C. Chen thanks the National Center for Theoretical Sciences in Taiwan for considerable help. This work is supported by the National Science Council (Grant No. NSC 95-2112-M-007-049-MY3) in Taiwan and the Boost project of the university.

[1] R. A. Webb, S. Washburn, C. P. Umbach, and R. B. Laibowitz, Phys. Rev. Lett. **54**, 2696 (1985).
[2] G. Timp, A. M. Chang, J. E. Cunningham, T. Y. Chang, P. Mankiewich, R. Behringer, and R. E. Howard, Phys. Rev. Lett. **58**, 2814 (1987).
[3] J. Liu, W. X. Gao, K. Ismail, K. Y. Lee, J. M. Hong, and S. Washburn, Phys. Rev. B **48**, 15148 (1993).
[4] E. Buks, R. Schuster, M. Heiblum, D. Mahalu, and V. Umansky, Nature (London) **391**, 871 (1998).
[5] B. Grbić, R. Leturcq, T. Ihn, K. Ensslin, D. Reuter, and A. D. Wieck, Phys. Rev. Lett. **99**, 176803 (2007).
[6] A. Yacoby, M. Heiblum, D. Mahalu, and H. Shtrikman, Phys. Rev. Lett. **74**, 4047 (1995).
[7] R. Schuster, E. Buks, M. Heiblum, D. Mahalu, V. Umansky, and H. Strikman, Nature (London) **385**, 417 (1997).
[8] M. Sigrist, T. Ihn, K. Ensslin, D. Loss, M. Reinwald, and W. Wegscheider, Phys. Rev. Lett. **96**, 036804 (2006).
[9] S. S. Buchholz, S. F. Fischer, U. Kunze, D. Reuter, and A. D. Wieck, Appl. Phys. Lett. **94**, 022107 (2009).
[10] J. J. Lin and J. P. Bird, J. Phys.: Condens. Matter **14**, R501-R596 (2002).
[11] F. P. Milliken, S. Washburn, C. P. Umbach, R. B. Laibowitz, and R. A. Webb, Phys. Rev. B **36**, 4465 (1987).
[12] S. Washburn, C. P. Umbach, R. B. Laibowitz, and R. A. Webb, Phys. Rev. B **32**, 4789 (1985).
[13] B. L. Altshuler, A. G. Aronov, and D. Khmelnitskii, J. Phys. C **15**, 7367 (1982).
[14] M. Büttiker, IBM J. Res. Dev. **32**, 317 (1988).
[15] G. Seelig and M. Büttiker, Phys. Rev. B **64**, 245313 (2001).
[16] J. P. Bird, K. Ishibashi, D. K. Ferry, Y. Ochiai, Y. Aoyagi, and T. Sugano, Phys. Rev. B **51**, 18037 (1995).
[17] R. M. Clarke, I. H. Chan, C. M. Marcus, C. I. Duruöz, J. S. Harris, K. Campman, and A. C. Gossard, Phys. Rev. B **52**, 2656 (1995).
[18] A. G. Huibers, M. Switkes, C. M. Marcus, K. Campman, and A. C. Gossard, Phys. Rev. Lett. **81**, 200 (1998).
[19] D. P. Pivin, A. Andresen, J. P. Bird, and D. K. Ferry, Phys. Rev. Lett. **82**, 4687 (1999).
[20] A. G. Huibers, J. A. Folk, S. R. Patel, C. M. Marcus, C. I. Duruöz, and J. S. Harris, Jr., Phys. Rev. Lett. **83**, 5090-5093 (1999).
[21] Y. Yamauchi, M. Hashisaka, S. Nakamura, K. Chida, S. Kasai, T. Ono, R. Leturcq, K. Ensslin, D. C. Driscoll, A. C. Gossard, and K. Kobayashi, Phys. Rev. B **79**, 161306(R) (2009).
[22] M. Cassé, Z. D. Kvon, G. M. Gusev, E. B. Olshanetskii, L. V. Litvin, A. V. Plotnikov, D. K. Maude, and J. C. Portal, Phys. Rev. B **62**, 2624 (2000).
[23] A. E. Hansen, A. Kristensen, S. Pedersen, C. B. Sorensen, and P. E. Lindelof, Phys. Rev. B **64**, 045327 (2001).
[24] K. Kobayashi, H. Aikawa, S. Katsumoto, and Y. Iye, J. Phys. Soc. Jpn. **71**, 2094 (2002).
[25] G. Seelig, S. Pilgram, A. N. Jordan, and M. Büttiker, Phys. Rev. B. **68**, 161310(R) (2003).
[26] M. Büttiker, Y. Imry, R. Landauer, and S. Pinhas, Phys. Rev. B **31**, 6207 (1985).
[27] M. Büttiker, Phys. Rev. Lett. **57**, 1761 (1986).
[28] G. Cernicchiaro, T. Martin, K. Hasselbach, D. Mailly, and A. Benoit, Phys. Rev. Lett. **79**, 273 (1997).
[29] G. Seelig, Ph.D. thesis, University of Geneva, 2003.
[30] V. S.-W. Chung, P. Samuelsson, and M. Büttiker, Phys. Rev. B **72**, 125320 (2005).
[31] L. S. Tan, S. J. Chua, and V. K. Arora, Phys. Rev. B **47**, 13868 (1993).
[32] K. Shepard, Phys. Rev. B **43**, 11623 (1991).